A Ring-Oscillator-Based Graphene Platform for Kinetic Discrimination at the Inner Helmholtz Layer

Babak Sharifi Taskuh[1]
[1] Department of Biomedical Engineering of Technical Engineering, Islamic Azad University, Sari Branch, Iran.
Corresponding author: Babak Sharifi Taskuh (e-mail: babak.sharifi@iau.ir , ORCID:0009-0002-5449-1696)

ABSTRACT

Graphene-based field-effect biosensors offer label-free detection of biomolecular binding, but sensitivity is fundamentally constrained by Debye screening at physiological ionic strength, and existing workarounds typically require bulky benchtop instrumentation such as impedance spectrometers. This paper proposes a fully electronic alternative: a differential ring oscillator in which graphene's quantum capacitance is placed in series with the Helmholtz and diffuse-layer capacitances of the sensing interface, converting interfacial capacitance dynamics directly into a continuously sampled oscillator frequency. Specific binding at the inner Helmholtz layer and bulk ionic screening proceed on very different timescales, and the platform discriminates between them from the time-domain shape of the frequency transient rather than its equilibrium value. A computational digital-twin framework, incorporating Langmuir binding kinetics and a combined shot/drift noise model, validated this principle on a synthetic dataset of specific-binding and bulk-screening events under 10-fold cross-validation. Rise time alone separates the two classes with 98.0% accuracy (AUC = 1.000), well ahead of the initial rate of frequency change considered on its own, while the complete feature set reaches 99.5% (SVM) and 99.3% (LDA) accuracy. These findings support timescale-resolved, frequency-domain readout as a route toward chip-scale, spectrometer-free biosensing, pending experimental validation on a fabricated device.

Keywords: *Digital Twin; Graphene Biosensor; Inner Helmholtz Layer; Quantum Capacitance; Ring Oscillator; Timescale Discrimination*

1. Introduction

Label-free electronic biosensing has increasingly turned to graphene field-effect transistors as a route to detecting biomolecules directly through their intrinsic charge, without fluorescent tags or optical labels. Yet this promise runs into a stubborn physical limit almost as soon as the sensor is placed in a realistic biological sample: at physiological ionic strength, the Debye screening length shrinks to sub-nanometer scale, so that the charge of a target molecule is electrostatically shielded from the transistor channel before it can be registered as a signal (Stern et al., 2007). A substantial body of work has responded by moving the measurement into the AC or radio-frequency domain, where mobile ions can no longer track the excitation fast enough to fully screen the interface, and has by this route partially recovered sensitivity that DC operation loses (Sarker et al., 2023). What these approaches share, however, is that they still report a single scalar quantity (an impedance magnitude, a capacitance, a shifted resonance) evaluated at or after equilibrium, and typically require bench-top instrumentation such as an electrochemical impedance spectrometer, incompatible with a portable, chip-scale platform.

A more basic gap follows from this. Even the approaches above distinguish a bound target from a purely resistive bulk medium, but they stop short of separating a specific binding event at the inner Helmholtz layer from a simultaneous, non-specific change in bulk ionic strength using the signal's time-domain shape, rather than its equilibrium magnitude. Sections II and IV develop the physical argument for why these two effects should unfold on very different timescales, and Section VI shows this distinction to be computationally recoverable. The separation comes primarily from how long the transient takes, not how steeply it begins.

This paper takes a different route: a graphene-integrated, differential ring oscillator in which the quantum capacitance of the graphene channel sits in series with the Helmholtz and diffuse-layer capacitances of the sensing interface, turning the oscillator's frequency into a continuously sampled readout of interfacial capacitance rather than a single post-hoc measurement. Specific binding and Debye-layer relaxation unfold on timescales that differ by orders of magnitude, and it is this gap that the platform is built to read, with no bench-top spectrometer in the loop.

The contributions of this work are as follows:

- A capacitive framework (Section II) that places graphene's quantum capacitance in series with an inner-Helmholtz-layer model, giving a physical basis for interfacial specificity absent from a conventional metal-electrode sensor.

- A differential ring-oscillator sensing architecture (Section III) that transduces this capacitance into a frequency signal while canceling common-mode drift, without dependence on bench-top impedance instrumentation.

- A timescale-based discrimination principle (Section IV), grounded in literature-reported binding kinetics, for separating specific binding at the inner Helmholtz layer from bulk ionic screening using the transient shape of the oscillator output.

- A computational digital-twin validation (Sections V–VI) identifying rise time, not the initial rate of change, as the dominant discriminating feature, reaching 98.0% classification accuracy alone and 99.5% in combination with complementary features, under a physiologically motivated noise model.

2. Concept and Physical Principle

Fig. 1 traces the signal chain this platform relies on, from a biomolecule approaching the graphene surface through to the frequency output of the oscillator circuit built around it in Section III.

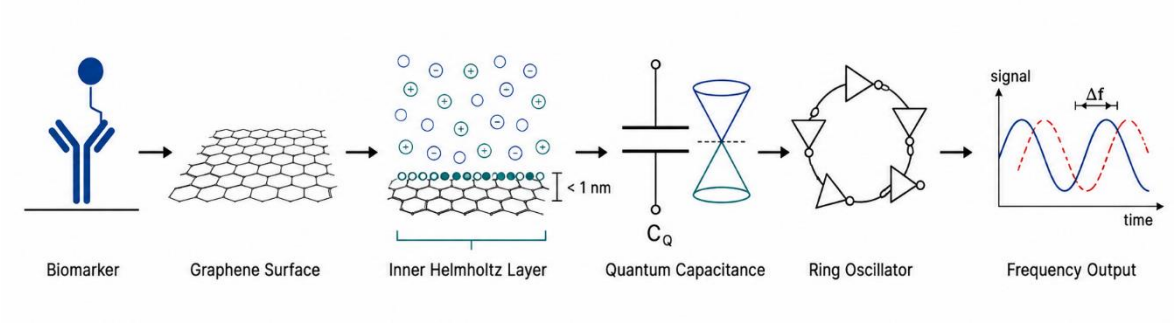


Figure 1. Conceptual signal chain: biomarker → graphene surface → inner Helmholtz layer → quantum capacitance → oscillator frequency.

At the heart of the platform sits a simple asymmetry. Unlike a conventional metal electrode, monolayer graphene has a linear, Dirac-like energy dispersion and a correspondingly low density of states near the charge-neutrality point. Integrating this density of states over the Fermi–Dirac distribution gives graphene's quantum capacitance in closed form (Fang et al., 2007), later confirmed by direct capacitance measurement (Xia et al., 2009):

$$C_Q(V_{ch}) = \frac{2e^2kT}{\pi(\hbar v_F)^2}\ln\left[2\left(1+\cosh\frac{eV_{ch}}{kT}\right)\right] \quad (1)$$

with $v_F \approx 10^6$ m/s the Fermi velocity and V_{ch} the channel potential measured from the Dirac point. At a representative operating point $V_{ch} = 0.10$ V and physiological temperature ($T = 310$ K), Eq. (1) evaluates to $C_Q \approx 2.4\ \mu F/cm^2$, on par with the capacitance of the adjacent electrolyte rather than dwarfed by it. That condition rarely holds for a metal electrode.

The interfacial side of this junction follows the classical Gouy–Chapman–Stern picture, which splits the electrical double layer into a compact, specifically adsorbed inner Helmholtz layer and an outer diffuse layer of hydrated ions. Graphene-specific treatments combining this picture with quantum capacitance have already been examined computationally in related electrochemical settings (Elliott et al., 2023). The inner layer, of thickness d_H on the order of a few angstroms, contributes

$$C_H = \frac{\varepsilon_H\,\varepsilon_0}{d_H} \quad (2)$$

while the diffuse layer contributes a potential- and ionic-strength-dependent capacitance given by the standard Gouy–Chapman expression. At physiological ionic strength (150 mM, 310 K), this places the Debye length at $\lambda_D \approx 0.80$ nm, matching the sub-nanometer screening regime noted in Section I (Stern et al., 2007), and combines with $C_H \approx 13.3\ \mu F/cm^2$ from Eq. (2) to give a diffuse-layer capacitance $C_{diff} \approx 96\ \mu F/cm^2$.

C_Q, C_H, and C_{diff} sit electrically in series (Zhan et al., 2015):

$$\frac{1}{C_{total}} = \frac{1}{C_Q} + \frac{1}{C_H} + \frac{1}{C_{diff}} \quad (3)$$

so the smallest of the three, C_Q in this case, sets C_{total}, which works out to roughly $2.0\ \mu F/cm^2$. We treat a specific binding event at the inner Helmholtz layer as a perturbation of C_H in Eq. (2), and a change in bulk ionic strength as acting on C_{diff} instead. That split is a simplification: a strongly redox-active or highly polarizable bound species could also shift C_Q directly through charge-transfer doping, an effect this model does not capture and one we return to in the Limitations discussion of Section VI. Within the approximation as stated, though, the two effects enter Eq. (3) through separate terms, and separate terms are what a kinetic discrimination scheme can tell apart.

3. Ring Oscillator Sensing Architecture

The series capacitance derived in Section II is only useful as a sensing quantity once it acts on something measurable. We embed it into the load of a CMOS ring oscillator: an odd number N of inverting delay stages in a closed loop, where one stage's load is the graphene–electrolyte interface itself instead of a fixed parasitic capacitance, so its output tracks $C_{total}(t)$ from Eq. (3) in real time.

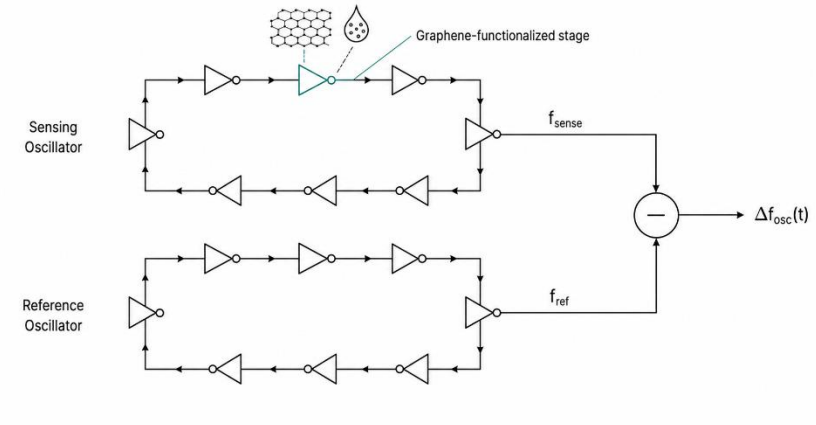


Figure 2. Ring oscillator with a graphene-functionalized sensing stage, paired with a reference (unexposed) oscillator branch for common-mode cancellation.

For a single stage under the standard RC-charging approximation, the propagation delay and resulting loop oscillation frequency are

$$\tau_d \approx 0.69\, R_{on}\, C_L\,, \qquad f_{osc} = \frac{1}{2N\tau_d} \quad (4)$$

where $C_L = C_{par} + C_{total}$ is the sensing stage's total load. Committing to specific values of R_{on}, electrode area, or C_{par} would mean assuming a fabrication process this study does not have, so instead we work with Eq. (4) in differential form. Since $f_{osc} \propto 1/C_L$, a small perturbation ΔC_{total} produces, to first order, a proportional fractional shift in oscillation frequency:

$$\frac{\Delta f_{osc}}{f_{osc}} \approx -\frac{\Delta C_{total}}{C_{par} + C_{total}} \quad (5)$$

The digital-twin framework of Section V evaluates this fractional form directly. It is converted to an absolute frequency only through an illustrative nominal carrier f_0 (Table 1), chosen for interpretability, not fitted to any fabricated device. The topology and differential-referencing principle follow established practice in capacitive ring-oscillator sensors (Kilpijärvi et al., 2018). That prior work is not graphene-based, and to our knowledge no graphene-integrated ring oscillator of this kind has been built before.

Table 1. Oscillator design parameters used in the digital-twin simulation.

Parameter	***Value***
*Number of stages, **N***	*15–31 (odd)*
Nominal carrier frequency, $\boldsymbol{f_0}$	*100 MHz (illustrative)*
Configuration	*Differential: sensing + unexposed reference*

A single oscillator would confuse the signal of interest with drift from temperature and supply-voltage fluctuations, both of which shift τ_d regardless of any surface event. Pairing the sensing oscillator with an identical reference oscillator on an unfunctionalized stage, then taking the difference of the two frequencies, is meant to cancel that common-mode drift. Section VI confirms this works: the differential trace $\Delta f_{osc}(t)$

recovers the underlying signal despite drift and shot noise injected independently into both branches. That differential trace is what the kinetic analysis in Section IV is built on.

4. Binding Kinetics and Timescale-Based Discrimination

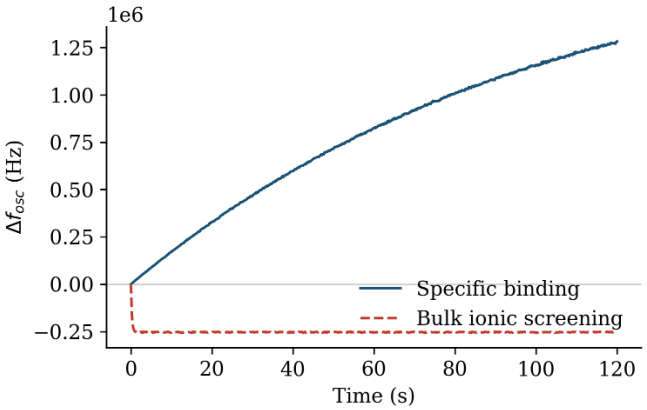


Figure 3. Simulated differential-oscillator transient for specific binding (solid) versus a bulk ionic-strength step (dashed); the classes separate mainly by settling time, not initial slope.

We model specific binding at the inner Helmholtz layer as a one-to-one Langmuir process, in which the fractional surface occupancy $\theta(t)$ *evolves as*

$$\frac{d\theta}{dt} = k_{on}C(1-\theta) - k_{off}\theta \quad (6)$$

with C *the analyte concentration and* k_{on}, k_{off} *the association and dissociation rate constants. These are broadly consistent with the spread of rates reported across large panels of antibody–antigen interactions characterized by SPR and label-free microarray assays (Landry et al., 2014). The framework does not depend on the specific receptor chemistry; aptamer-based recognition works equally well, provided the rate constants are comparable. Each bound molecule perturbs the inner-layer capacitance as*

$$C_H(t) = C_H^0\left(1 - \Delta_{frac}\,\theta(t)\right) \quad (7)$$

which propagates through Eq. (3) into the oscillator's differential frequency trace via Eq. (5).
Eq. (6) has a direct consequence: specific binding unfolds over a characteristic timescale

$$\tau_{bind} \sim \frac{1}{k_{on}C + k_{off}} \quad (8)$$

which can run from a few seconds to well beyond any practical observation window, depending on concentration and affinity. Bulk ionic-strength changes work differently. They act on C_{diff} *through Debye-layer relaxation, a process on the order of* $\tau_{ion} \sim 50 - 500$ *ms. That is three to five orders of magnitude faster than a typical binding event, and it lines up with the fast-relaxing, sub-nanometer screening layer discussed in Sections I and II (Stern et al., 2007).*
This gap in timescale, not the size of either signal, is what the platform is built to read. An EIS-based measurement takes Δf_{osc} *at one fixed later time; this sensor instead watches how the transient unfolds, in the same spirit as kinetic methods that separate surface-localized signals from bulk-refractive-index changes in other label-free platforms (Liu et al., 2021).*
In practice, how long the transient takes to reach its plateau (rise time) captures this gap more directly than its initial slope does, because τ_{bind} *often extends well past the earliest samples an initial-slope estimate*

would use. Section VI weighs both, alongside the total shift and its spectral content, and shows how much each one actually contributes. One caveat follows from this: the achievable separation depends on how the observation window compares to τ_{bind} and τ_{ion}, not on the timescale gap alone.

5. Computational Framework (Digital Twin)

No physical device has been fabricated for this study. The entire evaluation runs through a computational digital twin that instantiates the capacitive and kinetic models of Sections II–IV (Eqs. 1–7) as a working simulation of the proposed sensor, an approach with precedent in recent computational treatments of graphene-based biosensing (Baridi et al., 2026b). This is a deliberate choice, not a placeholder for future work: it makes every assumption traceable to a specific equation and lets the discrimination principle of Section IV be tested across hundreds of parameter combinations and independent noise realizations. What it does not yet capture is the device-specific non-idealities that only fabrication would reveal, a trade-off Section VI returns to directly.

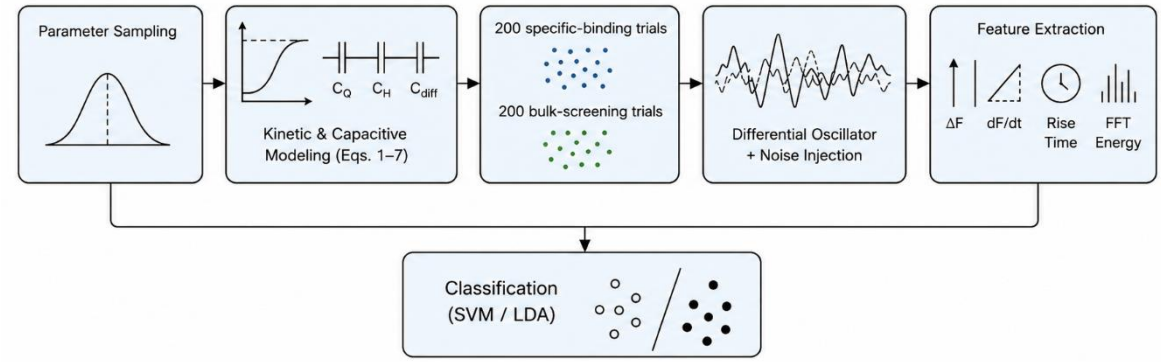


Figure 4. Digital-twin pipeline: parameter sampling → kinetic/capacitive modeling → differential-oscillator transduction with noise → feature extraction → classification

The physical and kinetic models were implemented in a MATLAB-compatible numerical environment (GNU Octave); the resulting feature vectors were passed to standard supervised classifiers (Section VI). For each of 200 trials per class (400 total), a parameter set — concentration C, rate constants k_{on} and k_{off}, and the fractional inner-layer perturbation Δ_{frac} — is drawn from the ranges in Table 2. Eqs. (1)–(7) are then evaluated forward in time at $f_s = 5$ Hz over a $T_{obs} = 120$ s window to produce a clean differential trace. Specific-binding trials follow the Langmuir rise of Eq. (6); bulk-screening trials instead apply a step change in ionic strength with a randomized onset relaxation τ_{ion}, consistent with the range motivated in Section IV. Both the sensing and reference oscillator branches (Section III) are then corrupted independently: Poisson-distributed shot noise reflects the discrete carrier statistics underlying C_Q, and slower Gaussian drift stands in for thermal and supply fluctuations. Taking their difference gives the composite trace a differential frequency counter would actually report, not an idealized curve.

Table 2. Digital-twin simulation parameters.

Parameter	***Range***
Concentration, $\boldsymbol{C}$	*1 nM – 1 μM (log-uniform)*
Association rate, $\boldsymbol{k_{on}}$	10^3–10^6 $M^{-1}s^{-1}$
Dissociation rate, $\boldsymbol{k_{off}}$	10^{-4}–10^{-2} s^{-1}
Ionic-step relaxation, $\boldsymbol{\tau_{ion}}$	*50–500 ms*
Sampling rate / window	*5 Hz / 120 s*
Noise model	*Poisson (shot) + Gaussian (drift)*
Trials	*200 per class, 400 total*

From each trace, four features are extracted: the total shift ΔF over the observation window; the initial slope dF/dt , estimated by linear fit over the first 5% of samples; the rise time to 90% of the eventual plateau, directly probing τ_{bind} as motivated in Section IV; and the FFT energy above the lower 20% of the spectrum, which picks up the sharper spectral signature of an abrupt ionic step against a smooth binding curve. Together, these four numbers are all Section VI has to work with.

6. Results and Discussion

The digital-twin framework of Section V was used to generate a balanced synthetic dataset of 400 trials (200 specific-binding, 200 bulk-ionic-screening events), evaluated under 10-fold stratified cross-validation with two classifiers: a support-vector machine (SVM, RBF kernel) and linear discriminant analysis (LDA).

6.1 Ablation Study

An ablation study isolates the contribution of each feature motivated in Sections IV–V.

Table 3. Ablation study: classification performance by feature (mean ± std over 10 folds).

Feature	SVM Accuracy	SVM AUC	LDA Accuracy	LDA AUC
dF/dt only	72.0 ± 7.9%	0.764 ± 0.085	45.8 ± 8.6%	0.586 ± 0.122
ΔF only	81.0 ± 6.4%	0.887 ± 0.064	54.3 ± 8.1%	0.676 ± 0.104
FFT energy only	84.0 ± 5.9%	0.889 ± 0.065	68.0 ± 5.5%	0.610 ± 0.094
Rise time only	98.0 ± 2.5%	1.000 ± 0.000	94.3 ± 3.9%	1.000 ± 0.000
All four (full)	99.5 ± 1.0%	1.000 ± 0.000	99.3 ± 1.2%	1.000 ± 0.000

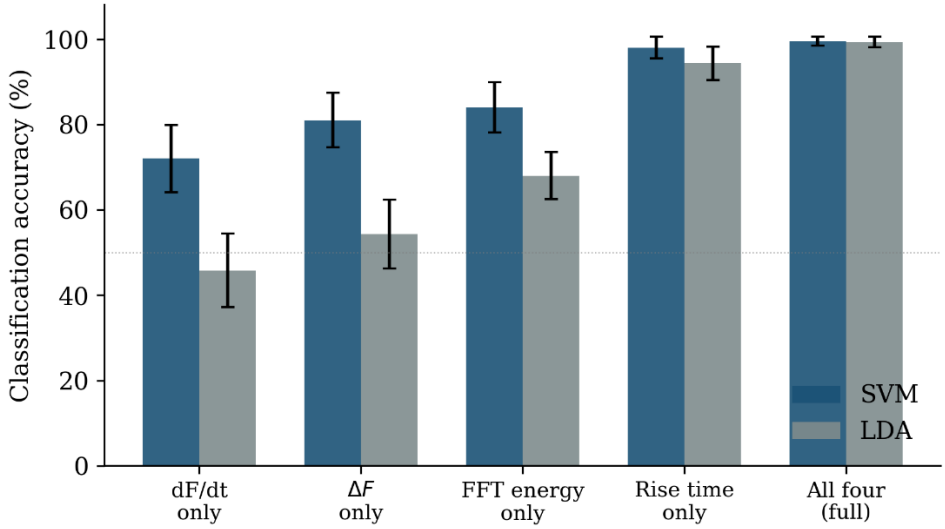


Figure 5. Classification accuracy by feature, showing the disproportionate contribution of rise time relative to the other three features considered individually.

A reading of Section IV focused narrowly on the earliest instant of the transient might expect dF/dt to carry most of the discriminating power. The ablation tells a more precise story. Alone, dF/dt is the weakest of the four (72.0% SVM). A slope estimated from the first 5% of the window is sensitive to shot noise, and for the slowest binding events Table 2 permits, the asymptotic slope has barely begun to emerge by the time it is measured. ΔF and FFT energy each recover a moderate, comparable amount of information (81.0% and 84.0%), consistent with an abrupt ionic step leaving both a distinct magnitude and a distinct spectral signature.

Rise time dominates. Alone, it reaches 98.0% accuracy and an AUC of 1.000 — the quantitative counterpart of the timescale argument in Section IV, where τ_{bind} and τ_{ion} sit orders of magnitude apart and rise time simply measures that gap most directly. The full four-feature set closes the remaining distance to 99.5%

(SVM) and 99.3% (LDA). SVM and LDA rest on very different decision boundaries, yet land within 0.2 percentage points of each other; that agreement points to a property of the underlying timescale separation, not an artifact of either classifier.

6.2 Comparison with Prior Work

Table 4. Comparison with representative label-free biosensing approaches.

Approach	***Detection Principle***	***Debye-Screening Immunity***	***Kinetic Discrimination***	***Instrument Footprint***
DC-operated GFET (Ono et al., 2024)	*Charge transfer at Dirac point*	*Limited*	*No*	*Portable*
EIS-based graphene sensor (Lopes et al., 2021)	*Interfacial impedance spectrum*	*Partial (frequency-dependent)*	*No*	*Bench-top spectrometer*
QCM (Yoshimine et al., 2023)	*Mass loading*	*N/A (not charge-based)*	*Limited*	*Portable*
Computational SPR (Baridi et al., 2026a)	*Refractive index, sensorgram kinetics*	*N/A (not charge-based)*	*Yes*	*Bench-top optical*
This work	*Quantum-capacitance-modulated oscillator*	*Addressed via kinetic readout*	*Yes (rise time)*	*Fully electronic, chip-scale*

Quantum-capacitance-modulated oscillators are not new on their own; resonant graphene sensors of this general type have already been demonstrated for vapor and humidity sensing (Deen et al., 2014). What is narrower here is the combination: a differential ring-oscillator topology in place of the earlier LC-tank designs, paired with a timescale-based discrimination scheme aimed at a distinction — specific binding versus bulk ionic screening — that those prior sensors were never built to make.

6.3 Limitations

All results above come from the computational framework of Section V. No device has been fabricated, and the model's kinetic and capacitive parameters, while drawn from literature-reported ranges, have not been measured for this specific geometry. Rise time's near-saturating performance is also partly an artifact of the setup: many binding trials never fully equilibrate within the fixed 120 s window, while the ionic step is constructed to resolve within about a second. Narrowing that gap would make for a harder, more informative test, and we leave it for future work. The problem as posed is also a clean two-class distinction; it excludes non-specific molecular interferents, which carry their own kinetics and could well overlap with either class. Finally, this study targets binary event-type discrimination rather than dose-response calibration, so no formal limit of detection has been established. Read these results as computational validation of a discrimination principle, not as measured analytical performance.

7. Conclusion

This paper set out to recast biosensing detection around the temporal shape of an interfacial capacitance transient, not a single equilibrium reading. Placing graphene's quantum capacitance in series with the Helmholtz and diffuse-layer capacitances of the sensing interface lets a differential oscillator pair turn binding events into a continuously sampled frequency trace, with no bench-top impedance spectrometer or scanning-probe instrument standing between the sample and the readout.
The central finding is timescale, not magnitude: specific binding and bulk ionic screening settle on characteristic timescales that differ by three to five orders of magnitude (τ_{bind} against a Debye-limited τ_{ion}),

and the transient's rise time captures that gap far better than its initial slope does. Rise time alone reached 98.0% classification accuracy in the digital-twin evaluation of Section VI; the full feature set pushed that to 99.5% (SVM) and 99.3% (LDA).

These numbers come from simulation, not a fabricated chip. The natural next step is building one — a device where τ_{bind} and τ_{ion} can be measured directly rather than modeled, with the observation window pulled in toward the regime where the two timescales genuinely compete.

REFERENCES

[1] *Baridi, G., Liaquat, A., Martini, L., Rapuzzi, F., Clericò, V., Amado, M., Diez, E., Abidi, E. H., Maschio, M. C., Corni, S., Meziani, Y. M., Brancolini, G., Rossella, F., & Rovati, L. (2026a). Computational simulation of a surface plasmonic resonance biosensor for β2-microglobulin based on electrolyte-gated graphene. Sensors, 26(9), 2815.* https://doi.org/10.3390/s26092815

[2] Baridi, G., Liaquat, A., Martini, L., Rapuzzi, F., Herath, H. M. K. G. A., Abidi, E. H., Maschio, M. C., Clericò, V., Meziani, Y. M., Amado, M., Diez, E., Corni, S., Brancolini, G., Rovati, L., & Rossella, F. (2026b). Multiscale molecular dynamics and quantum–electrostatic modelling of graphene electric double-layer transistors for β2-microglobulin biosensing. Electronics, 15(13), 2837. https://doi.org/10.3390/electronics15132837

[3] Deen, D. A., Olson, E. J., Ebrish, M. A., & Koester, S. J. (2014). Graphene-based quantum capacitance wireless vapor sensors. IEEE Sensors Journal, 14(5), 1459–1466. https://doi.org/10.1109/JSEN.2013.2295302

[4] Elliott, J. D., Chiricotto, M., Troisi, A., & Carbone, P. (2023). Do specific ion effects influence the physical chemistry of aqueous graphene-based supercapacitors? Perspectives from multiscale QMMD simulations. Carbon, 207, 292–304. https://doi.org/10.1016/j.carbon.2023.03.019

[5] Fang, T., Konar, A., Xing, H., & Jena, D. (2007). Carrier statistics and quantum capacitance of graphene sheets and ribbons. Applied Physics Letters, 91(9), 092109. https://doi.org/10.1063/1.2776887

[6] Kilpijärvi, J., Halonen, N., Sobocinski, M., Hassinen, A., Senevirathna, B., Uvdal, K., Abshire, P., Smela, E., Kellokumpu, S., Juuti, J., & Lloyd Spetz, A. (2018). LTCC packaged ring oscillator based sensor for evaluation of cell proliferation. Sensors, 18(10), 3346. https://doi.org/10.3390/s18103346

[7] Landry, J. P., et al. (2014). Measuring affinity constants of 1,450 monoclonal antibodies to peptide targets with a microarray-based label-free assay platform. Journal of Immunological Methods, 417, 86–96. https://doi.org/10.1016/j.jim.2014.12.011

[8] Liu, F., Zhang, X., Li, K., Guo, T., Ianoul, A., & Albert, J. (2021). Discrimination of bulk and surface refractive index change in plasmonic sensors with narrow bandwidth resonance combs. ACS Sensors, 6(8), 3013–3023. https://doi.org/10.1021/acssensors.1c00906

[9] Lopes, L. C., Santos, A., & Bueno, P. R. (2021). Measuring quantum conductance and capacitance of graphene using impedance-derived capacitance spectroscopy. Carbon, 184, 821–827. https://doi.org/10.1016/j.carbon.2021.08.055

[10] Ono, T., et al. (2024). Challenges for field-effect-transistor-based graphene biosensors. Materials, 17(2), 333. https://doi.org/10.3390/ma17020333

[11] Sarker, B. K., Shrestha, R., Singh, K. M., Lombardi, J., An, R., Islam, A., & Drummy, L. F. (2023). Label-free neuropeptide detection beyond the Debye length limit. ACS Nano, 17(21), 20968–20978. https://doi.org/10.1021/acsnano.3c02537

[12] Stern, E., Wagner, R., Sigworth, F. J., Breaker, R., Fahmy, T. M., & Reed, M. A. (2007). Importance of the Debye screening length on nanowire field effect transistor sensors. Nano Letters, 7(11), 3405–3409. https://doi.org/10.1021/nl071792z

[13] Xia, J., Chen, F., Li, J., & Tao, N. (2009). Measurement of the quantum capacitance of graphene. Nature Nanotechnology, 4, 505–509. https://doi.org/10.1038/nnano.2009.177

[14] Yoshimine, H., Sasaki, K., & Furusawa, H. (2023). Pocketable biosensor based on quartz-crystal microbalance and its application to DNA detection. Sensors, 23(1), 281. https://doi.org/10.3390/s23010281

Zhan, C., Neal, J., Wu, J., & Jiang, D.-E. (2015). Quantum effects on the capacitance of graphene-based electrodes. The Journal of Physical Chemistry C, 119(39), 22297–22303. https://doi.org/10.1021/acs.jpcc.5b05930